



# Preparation and characterization of $\text{Bi}_2\text{Se}_3(0001)$ and of epitaxial FeSe nanocrystals on $\text{Bi}_2\text{Se}_3(0001)$



Alberto Cavallin, Vasilii Sevriuk, Kenia Novakoski Fischer, Sujit Manna, Safia Ouazi, Martin Ellguth, Christian Tusche, Holger L. Meyerheim, Dirk Sander\*, Jürgen Kirschner

Max-Planck-Institut für Mikrostrukturphysik, Weinberg 2, 06120 Halle, Germany

## ARTICLE INFO

Available online 11 September 2015

### Keywords:

Bismuth selenide  
Iron selenide

## ABSTRACT

Procedures to prepare clean  $\text{Bi}_2\text{Se}_3(0001)$  surfaces from bulk samples and epitaxial FeSe nanocrystals on  $\text{Bi}_2\text{Se}_3(0001)$  are reported.  $\text{Bi}_2\text{Se}_3(0001)$  substrates are prepared by *in vacuo* cleavage of bulk samples, followed by ion bombardment and annealing cycles. FeSe is prepared by Fe deposition onto  $\text{Bi}_2\text{Se}_3$  at 303 K, followed by annealing at  $T \approx 623$  K. We use low-energy electron diffraction, surface X-ray diffraction, photoemission spectroscopy, scanning tunneling microscopy and spectroscopy, and stress measurements to elucidate the correlation between structural and electronic properties of the pristine  $\text{Bi}_2\text{Se}_3(0001)$  and FeSe covered surfaces. Our analysis reveals the formation of epitaxial FeSe nanocrystals with a thickness of three unit cells (1.5 nm). Electron diffraction experiments indicate an anisotropic epitaxial strain in FeSe. A negligible strain close to 0.0% and a tensile strain of +2.1% are observed along the in-plane  $[01\bar{1}0]$  and  $[2\bar{1}\bar{1}0]$   $\text{Bi}_2\text{Se}_3$  directions, respectively. The out-of-plane strain is +4.2%. The role of this strain state for the reported high- $T_C$  superconductivity in bulk FeSe is discussed.

© 2015 Elsevier B.V. All rights reserved.

## 1. Introduction

Intriguingly complex physical properties emerge at the interfaces between Fe-based superconductors and topological insulators [1,2]. FeSe and  $\text{Bi}_2\text{Se}_3$  are prototypes of the former and latter material class, respectively. Proximity effects in superconductivity, charge transfer, interface stress, spin-orbit coupling, and crystal field effects have been reported. These properties may prove essential for applications in quantum computation [3]. A critical aspect in their realization is the formation of well-characterized interfaces.

We present procedures to obtain FeSe nanocrystals with a thickness of a few unit cells on the (0001) surface of the topological insulator  $\text{Bi}_2\text{Se}_3$  by epitaxial growth. This system represents a model case to study structural and electronic aspects at the interface between a topological insulator and FeSe, which is an unconventional superconductor in its bulk phase.

A multi-technique surface science study is applied to identify electronic and structural properties of  $\text{Bi}_2\text{Se}_3$ -supported FeSe nanocrystals, where scanning tunneling microscopy and spectroscopy (STM, STS), low-energy electron diffraction (LEED), photoemission electron microscopy (PEEM), photoemission electron spectroscopy, surface X-ray diffraction (SXRD) and optical two-beam curvature stress measurement are employed.

Cleavage of layered substrate materials, such as  $\text{Bi}_2\text{Se}_3$ , is an established preparation technique [4,5,6]. However, for 0.1 mm thin substrates used in curvature stress measurements, it becomes impractical. Therefore, we used ion bombardment and annealing of

bulk  $\text{Bi}_2\text{Se}_3(0001)$  samples as an alternative preparation technique. This procedure led to surfaces which compared favorably to samples cleaved *in vacuo* both in view of the morphology and of the low density of impurities at the surface.

Furthermore, we provide experimental evidence from several complementary surface sensitive techniques that epitaxial FeSe is obtained on  $\text{Bi}_2\text{Se}_3$  upon annealing of room temperature deposited Fe atoms. Our results indicate a non-trivial growth mode, where FeSe nanocrystals with an anisotropic strain state are embedded in the  $\text{Bi}_2\text{Se}_3(0001)$  surface.

## 2. Sample preparation—General aspects

Starting point of our studies are  $\text{Bi}_2\text{Se}_3(0001)$  single crystals, which were grown by the Bridgman method. The lattice constants of bulk  $\text{Bi}_2\text{Se}_3$  are in the basal plane  $a = 4.14$  Å and along the c-axis  $c = 28.64$  Å. We use samples with a lateral size of  $7 \times 7$  mm<sup>2</sup> and an approximate thickness of 0.5 mm, which we cleave *in vacuo* or, alternatively, prepare by ion bombardment and annealing. For photoemission experiments, the samples are glued to a Mo sample holder with a graphitic adhesive (Resbond 931C from Polytec PT [7]). In STM experiments, the  $\text{Bi}_2\text{Se}_3$  sample is glued on a copper spacer, fixed to a STM sample plate. For curvature stress measurements, samples are cleaved from bulk  $\text{Bi}_2\text{Se}_3(0001)$  single crystals to be 12 mm long, 2–3 mm wide and roughly 0.1 mm thin. They are carefully clamped along their width at one side to the sample manipulator to enable a free 2-dimensional stress-induced substrate curvature.

\* Corresponding author.

Fig. 1 illustrates the cleavage procedure: A copper cylinder is glued to the surface of a  $\text{Bi}_2\text{Se}_3$  crystal which itself is glued to a Mo sample holder, both using a graphitic adhesive. Before cleaving, the sample with the copper cylinder is rotated to face downwards. A wobble stick is used inside the ultra-high vacuum (UHV) chamber to gently press against the Cu cylinder, while the sample holder is kept in a fixed position. The resulting torque leads to a smooth cleavage of the  $\text{Bi}_2\text{Se}_3$  crystal, and the Cu cylinder automatically moves away from the freshly cleaved surface. This configuration allows reliable *in vacuo* cleavage.

In addition to samples cleaved *in vacuo*, we also studied  $\text{Bi}_2\text{Se}_3$  samples cleaved in air, which subsequently have been exposed to Ar-ion bombardment (energy: 1–2 keV, sample current density:  $\approx 0.1 \mu\text{Amm}^{-2}$ , for 15 min) and annealing cycles. The annealing temperature is a critical parameter, and this aspect is elucidated further in the Appendix A.

The temperature was measured at the sample holder by a type-K thermocouple and independently checked by an infra-red thermometer (IMPAC 140 [8]), to ensure that the sample temperature never exceeded 753 K during heat treatments. After keeping  $\text{Bi}_2\text{Se}_3$  crystals above this temperature for 10–30 min, we observed a loss of the optical reflectivity, and an irreversible change of the electronic structure.

Fe was deposited onto the  $\text{Bi}_2\text{Se}_3$  surface at room temperature by thermal evaporation from a 99.995% purity rod at a rate of approximately 0.5 ML (ML: monolayer) per minute, as checked by a quartz microbalance and cross-checked by surface coverage studies on single crystal metal substrates by STM. We define 1 ML as a single layer Fe with a surface atomic density of the  $\text{Bi}_2\text{Se}_3(0001)$  surface. The surface unit cell of  $\text{Bi}_2\text{Se}_3$  has a size of  $4.14^2 \text{ \AA}^2 \sin(120^\circ)$ , corresponding to an areal atomic density of 1 ML:  $6.74 \times 10^{14} \text{ cm}^{-2}$ .

We produce FeSe nanocrystals by post-deposition annealing at 623 K for 50 min in all experiments, except for curvature stress measurements. There, FeSe is formed by Fe deposition onto a  $\text{Bi}_2\text{Se}_3$  substrate held at an elevated temperature of 473 K.

For XRD experiments, we employed a UHV diffractometer equipped with a microfocus X-ray source (Cu-K $\alpha$  radiation) and a two-dimensional pixel detector [9]. Momentum-resolved photoemission data and PEEM images were acquired with a momentum microscope as described in [10]. For the photoemission experiments we illuminate the sample either by the He-I line from a focussed gas discharge lamp (Specs UVS-300) or by 6 eV photons from the fourth

harmonics of a Ti:Sa laser system. In PEEM experiments a Hg–Xe discharge lamp ( $h\nu = 5.9 \text{ eV}$ ) is used.

All STM studies are carried out at 10 K. We used electrochemically etched tungsten tips [11]. STS measurements were performed by a lock-in technique with a modulation frequency of 4.6 kHz and  $V_{\text{osc}} = 5 \text{ mV}$  modulation amplitude, applied to the gap voltage [12].

In all experiments Auger electron spectroscopy (AES) and low-energy electron diffraction (LEED) were performed by dedicated AES-spectrometers and LEED-optics to characterize the chemical composition and the structure of the sample surfaces.

### 3. Preparation and characterization of the $\text{Bi}_2\text{Se}_3(0001)$ surface—STM and photoemission experiments

The suitability of  $\text{Bi}_2\text{Se}_3$  for cleaving is due to its layered atomic structure. Cleaving occurs between van-der-Waals (vdW) bonded quintuple layers (QL) [13], each characterized by a Se–Bi–Se–Bi–Se layer sequence. After cleaving, atomically flat terraces are obtained, separated by steps that have a height of a quintuple layer (QL: 9.5  $\text{\AA}$ ), see also Fig. 3(a). We present in Fig. 2(a) a constant-current STM image of an as-cleaved  $\text{Bi}_2\text{Se}_3(0001)$  surface, which has not been ion-bombarded. The image reveals an atomically flat and clean surface with a few protrusions (apparent height  $\leq 20 \text{ pm}$ ). They are ascribed to subsurface defects [4,14]. Fig. 2(b) shows a zoom-in, which reveals the atomic corrugation. The hexagonal surface unit cell with base vectors of length  $a = 4.14 \text{ \AA}$  is indicated.

We observe broad LEED spots for samples which were prepared by ion bombardment and annealing at a low temperature of  $T_{\text{ann}} < 623 \text{ K}$ , indicative of a reduced crystallographic long-range order. Under these conditions, an unexpected long-range quasi-hexagonal superstructure appears, as detected by STM. This finding is discussed in the Appendix A.

We find that annealing of ion bombarded samples to  $T_{\text{ann}} = 673\text{--}693 \text{ K}$  gives good results, and a typical resulting STM image is presented in Fig. 3. Fig. 3(a) shows a large scale image of terraces, separated by a QL step (0.95 nm), as revealed in the line scan of (b). A zoom-in (c) shows a terrace with some protrusions with an apparent height of 70 pm. We ascribe the protrusions tentatively to adatoms, possibly due to surface contaminations. Their density corresponds to a surface coverage of 0.5%. We cannot confirm the presence of carbon by AES, as the surface coverage is too low. We speculate that the protrusions could be due to Bi, Se or carbon, which is common sources of contamination for this system [15]. Further studies are called for to clearly identify the atomic nature of these protrusions.

The zoom-in in Fig. 3(d) reveals the atomic corrugation indicative of clean  $\text{Bi}_2\text{Se}_3(0001)$ , as shown above for the *in vacuo* cleaved-only preparation in Fig. 2(b). On the atomic level, the structural uniformity is interrupted by subsurface defects, comparable to those found for the cleaved  $\text{Bi}_2\text{Se}_3$  sample, shown in Fig. 2(a). These defects have been reported before, and they are ascribed to point defects below the topmost surface [4,14].

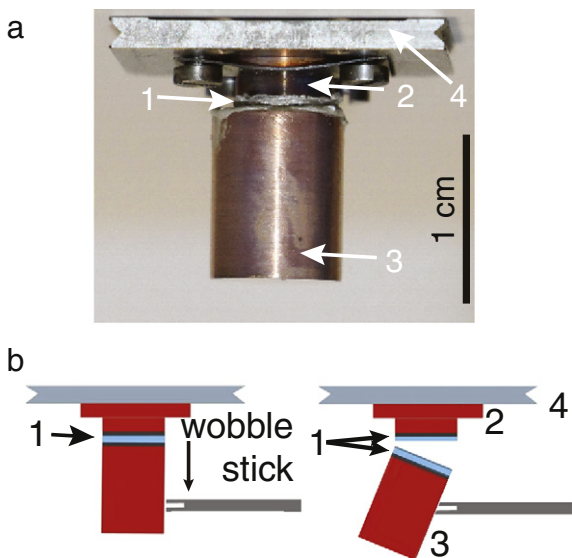


Fig. 1. (a) Photograph of the mounted sample prepared for the cleaving procedure: a  $\text{Bi}_2\text{Se}_3$  crystal (1) is glued between a Cu spacer (2) and a Cu cylinder (3). These parts are supported by a Mo STM sample plate (4). (b) The schematic shows the *in vacuo* sample cleaving by pressing a wobble stick against the Cu cylinder.

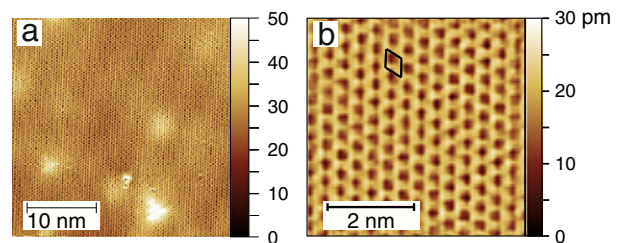
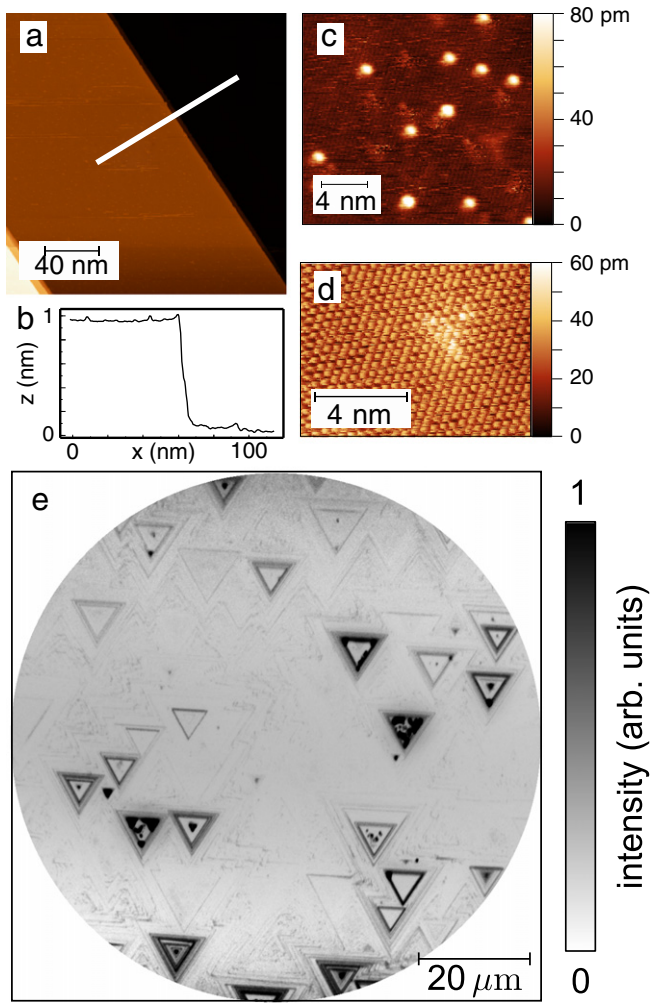


Fig. 2. STM image of *in vacuo* cleaved  $\text{Bi}_2\text{Se}_3$ . Protrusions appear which are 15 or 30 pm high, see [5]. (a) Atomically resolved surface structure of  $\text{Bi}_2\text{Se}_3(0001)$ , (b) zoom-in of the top part of (a), black lines indicate the surface unit cell. Scanning parameters:  $U = -0.1 \text{ V}$ ,  $I_t = 1 \text{ nA}$ .



**Fig. 3.** STM images of a sputtered and annealed  $T_{\text{ann}} = 673\text{--}693$  K sample. (a) Large scale STM constant current image.  $U = +0.7$  V,  $I_T = 0.5$  nA. An apparent height profile along the white line is shown in (b). It reveals a step height of 0.95 nm. (c) Zoom-in,  $U = +0.4$  V,  $I_T = 0.2$  nA. (d) Zoom-in,  $U = -0.4$  V,  $I_T = 0.15$  nA. (e) Clean  $\text{Bi}_2\text{Se}_3$  surface imaged on a mesoscopic scale by energy-filtered photoemission electron microscopy (PEEM) using a Hg–Xe discharge lamp ( $h\nu = 5.9$  eV). The energy window was set to emission threshold (lowest kinetic energy) exploiting the spatial variation of the work function for highest contrast.

Fig. 3(e) shows the surface morphology of the  $\text{Bi}_2\text{Se}_3$  single crystal on a mesoscopic scale. The PEEM image reveals that the preparation leads to the formation of mesoscopic flat surface regions and of triangular islands, which all show the same rotational alignment. This observation confirms the long-range crystalline order within the field of view of Fig. 3(e) and beyond. The PEEM image was recorded at a fixed final state energy of the photoelectrons at  $E - E_F = 5.38$  eV above the Fermi energy, using the energy filter of the momentum microscope instrument [10]. Here, the energy resolution was set to 60 meV. This allows us to identify the contrast mechanism in the PEEM image. The selected energy is slightly below the work function of  $\text{Bi}_2\text{Se}_3$  (5.61 eV), and clean  $\text{Bi}_2\text{Se}_3$  appears white (low intensity).

The mesoscopic islands consist of an aggregation of a possible large number of step edges, which are aligned along the principal in-plane crystal directions. The contrast in the PEEM image is ascribed to adsorbates, decorating step edges. This lowers locally the work function, giving rise to an enhanced electron emission.

Note that some of the triangular objects enclose an area of constant intensity, which equals that of the surroundings. We ascribe this to flat

terraces of few  $\mu\text{m}$  size, which are at a higher or lower level as compared to the average height of the crystal surface. In between the islands, flat terraces with diameters of several tenth of  $\mu\text{m}$  are observed.

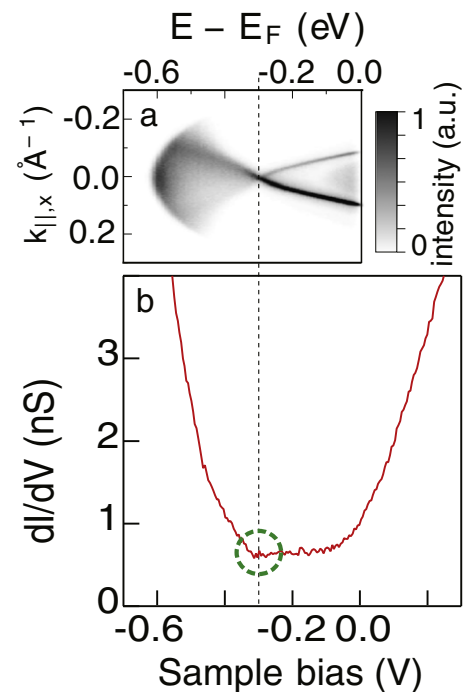
To perform our momentum-resolved photoemission experiments, the irradiated area which contributes to the spectra has a diameter of typically 20  $\mu\text{m}$  or less. The area was chosen within a flat terrace, as identified by PEEM. This alignment allowed for a representative mapping of the electronic structure of flat surface regions, yielding well-defined patterns in the momentum distribution of the photocurrent.

Fig. 4(a) presents  $k_{\parallel}$ -resolved photoemission data of the sample, using p-polarized light with a photon energy of 6.0 eV. The spectroscopy reveals the hallmark of the topological surface state of  $\text{Bi}_2\text{Se}_3$  [16]. The image shows an intensity distribution with two branches. They indicate a linear electron dispersion for energies above  $-0.3$  eV. We identify the crossing point of the two branches as the Dirac point ( $D_P$ ) at  $-0.3$  eV below the Fermi level. This energetic location of the  $D_P$  corresponds to the intrinsic n-doping related to selenium defects.

Fig. 4(b) shows the differential conductance  $dI/dV$  measured by STS on the sample shown in Fig. 3(b), away from the protrusions. We find that the  $dI/dV$  signal increases sharply below  $-0.3$  V and above 0 V sample bias. Between these gap voltages we observe a fairly constant signal. To compare the STS  $dI/dV$  data in Fig. 4(b) with our photoemission data we recall that the differential conductivity collected in STS can be ascribed to the momentum-integrated density of states (DOS). Integration of the photoemission data of the linearly dispersing state in momentum space yields a constant DOS, and this corresponds to the constant STS data in this energy range. Also, the Dirac point at  $-300$  meV appears as a shallow dip in STS, as previously reported [4].

#### 4. Formation of FeSe nanocrystals on $\text{Bi}_2\text{Se}_3(0001)$

In the following section we present the morphological, structural and electronic properties of FeSe nanocrystals prepared on  $\text{Bi}_2\text{Se}_3(0001)$ .



**Fig. 4.** (a) Photoemission electron spectroscopy on the sample characterized in Fig. 3. It shows the linearly dispersing surface states crossing at the Dirac point near  $-0.3$  eV and (b) STS of  $\text{Bi}_2\text{Se}_3$  with a shallow dip at the Dirac point (marked by the green circle).

#### 4.1. STM results—FeSe morphology and atomic corrugation

The STM image of Fig. 5 is measured after deposition of  $\approx 0.7$  ML of Fe on  $\text{Bi}_2\text{Se}_3$  at room temperature and heating to 628 K for 10 min. Fig. 5 is a large-scale STM image, which reveals the coexistence of  $\text{Bi}_2\text{Se}_3$  and FeSe regions, as labeled in the image. The regions of  $\text{Bi}_2\text{Se}_3$  and FeSe are identified by the atomic corrugation and symmetry of the surface, which are different for both phases. Atomically resolved STM on the  $\text{Bi}_2\text{Se}_3$ (0001) phase reveals a surface unit cell with an angle of  $60^\circ$  between the surface unit vectors, which have a length of approximately 4.14 Å. Corresponding measurements on FeSe reveal orthogonal surface unit cell vectors of almost equal length of approximately 3.8 Å. Our quantitative analysis of the FeSe covered surface by LEED identifies a rectangular surface unit cell for FeSe where the unit cell vectors  $a$  and  $b$  differ by 2%, as outlined below. This minute deviation from an apparent square surface unit cell in FeSe is hard to identify reliably by atomically-resolved STM, as shown in Fig. 6.

Fig. 5 shows mostly elongated FeSe islands, with lateral extension exceeding a few hundred nm. Their orientation suggests a preferential growth along axes, which are rotated by multiples of  $60^\circ$  from each other, revealing the  $p3m1$  symmetry of the underlying substrate surface. A close inspection of the height levels of FeSe suggests, that FeSe nanocrystals are formed, which are embedded in the  $\text{Bi}_2\text{Se}_3$  surface, as discussed below in Fig. 13. The sketch of Fig. 13 indicates that FeSe is embedded by one quintuple layer of  $\text{Bi}_2\text{Se}_3$  into the surface. This represents the situation for FeSe (green) imaged in the lower left part of Fig. 5. However, also non-integer embedding depths in units of

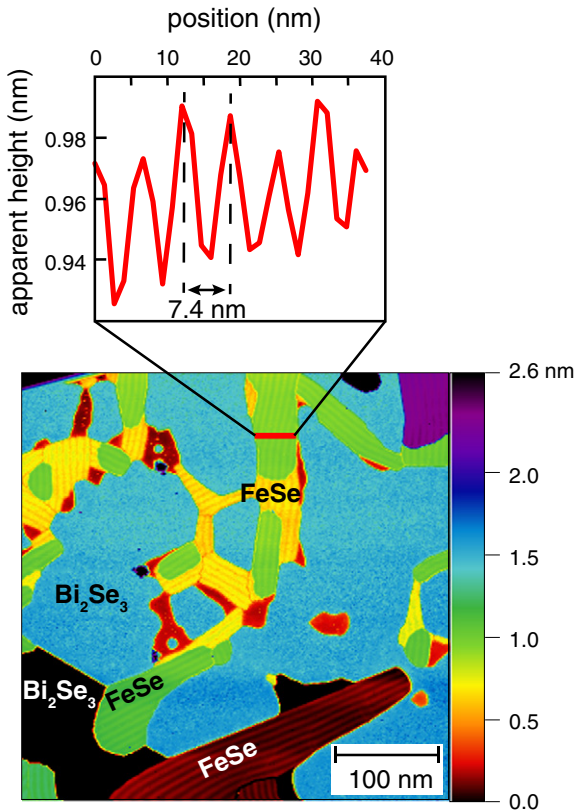


**Fig. 5.** Large-scale, constant-current STM image of FeSe nanocrystals grown on  $\text{Bi}_2\text{Se}_3$ (0001). Terraces of  $\text{Bi}_2\text{Se}_3$ , separated by QL height steps (0.95 nm), and smaller step heights between  $\text{Bi}_2\text{Se}_3$  and FeSe regions are observed. The FeSe regions show a stripe contrast in the apparent height, which is revealed by the line profile through a FeSe island at the top of the image.  $\text{Bi}_2\text{Se}_3$  and FeSe regions are identified by atomically resolved STM, see text for details. Red patches are ascribed to  $\text{Bi}_2\text{Se}_3$  regions, where smaller than QL height steps are observed.  $U = -0.3$  V,  $I_T = 1$  nA.

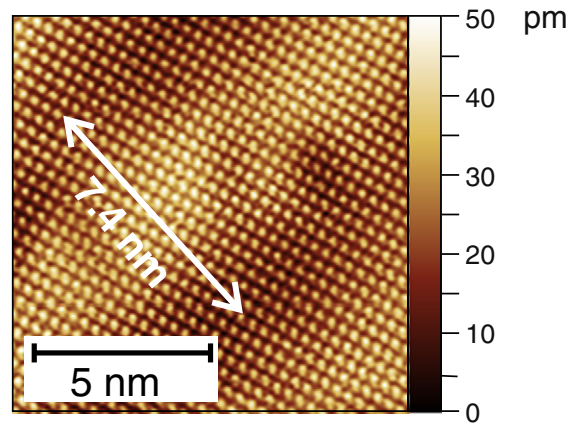


**Fig. 6.** Atomically-resolved STM image of FeSe on  $\text{Bi}_2\text{Se}_3$ (0001). The stripe pattern appears as a 7.4 nm periodic modulation of the apparent height. The amplitude of this modulation is  $\approx 20$  pm. Image parameters:  $U = +0.3$  V,  $I_T = 0.2$  nA.

quintuple layer thickness are observed, and this depth distribution is characteristic for the chosen annealing temperature.

Another important finding of the STM study is the observation of a stripe contrast on the FeSe islands. We ascribe the stripe pattern to a Moiré superlattice, as discussed in Section 5.1 below, and which has been observed before in the related system  $\text{Bi}_2\text{Se}_3$  on FeSe [17]. The line scan in Fig. 5 reveals a length of 7.4 nm for the spatial periodicity of the stripe contrast.

The zoom-in into a FeSe region in Fig. 6 shows the atomic corrugation indicative of the surface unit cell symmetry of FeSe, and it gives the periodicity of the stripe pattern. We point out that no surface defects are apparent in STM, and we ascribe this to the structural coherency of the FeSe nanocrystals, leading to either FeSe or  $\text{Bi}_2\text{Se}_3$  areas.

Atomic resolution STM images of FeSe regions, see Fig. 6, reveal an approximately square lattice with a periodicity of 3.8 Å. This compares favorably with the bulk lattice constant of FeSe of 3.77 Å [18,19]. The spatial modulation with a periodicity of 7.4 nm, mentioned above (see line scan in Fig. 5) is indicated in Fig. 6. The vertical amplitude of this apparent height modulation is  $\approx 20$  pm. The stripe directions are predominantly aligned along the long direction of the FeSe regions. A thorough discussion of this long-range periodicity is presented in Section 5.

#### 4.2. Structural characterization: LEED and SXRD

The inspection of the LEED pattern provides quantitative information on the metric of the adlayer relative to that of the substrate. Fig. 7(a) shows the LEED pattern of the pristine  $\text{Bi}_2\text{Se}_3$ (0001) surface. A trigonal arrangement of diffraction spots reflects the  $p3m1$  plane group symmetry of the  $\text{Bi}_2\text{Se}_3$ (0001) surface. Fig. 7(b) reveals that deposition of 0.7 ML Fe and subsequent annealing leads to the appearance of additional diffraction spots, which we ascribe to the formation of FeSe in three rotational domains. The unit cells of the respective domains are indicated by different colors in Fig. 7(b). This assessment is supported by the analysis and discussion of the position of higher-order diffraction spots in Section 5.

X-ray diffraction experiments are performed to measure the thickness of the FeSe regions for the preparation as described above. The scattered X-ray intensity along (01l) and (02l) rods is measured, and the result is presented in Fig. 8. Here, the peak positions at  $q_z = 4.93$  and 5.05 r.l.u. (reciprocal lattice unit, 1 r.l.u. =  $(28.64 \text{ Å})^{-1}$ ) for the first and second order rods, respectively, indicate an average lattice constant along the out-of-plane direction of 5.73 Å. This is 4% expanded with respect to the FeSe bulk value of 5.51 Å [18,20]. The full width at half maximum (FWHM) of the reflection profile is inversely proportional to the film thickness,  $t$ , given by  $t = \frac{0.886}{\text{FWHM}[\text{Å}^{-1}]}$  [21]. The peaks of the

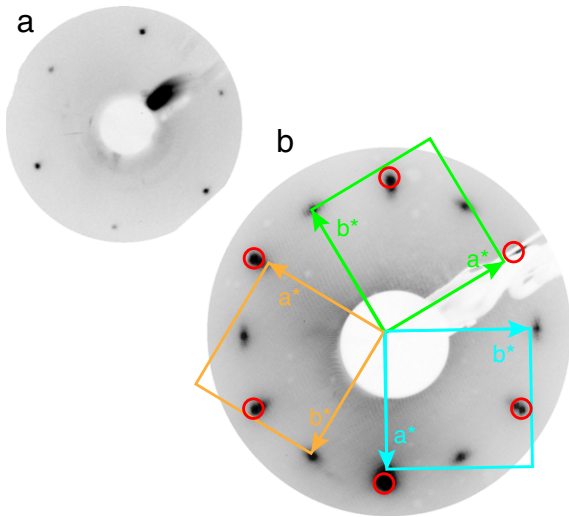


**Fig. 7.** LEED pattern of  $\text{Bi}_2\text{Se}_3$ , 38 eV (a), and of  $\text{FeSe}/\text{Bi}_2\text{Se}_3$ , 51 eV (b). All diffraction spots in (a) and those circled in red in (b) are first order  $\text{Bi}_2\text{Se}_3$  reflections. The remaining spots are due to FeSe. These spots are ascribed to three domain orientations. The corresponding reciprocal space unit vectors are shown in yellow, green, and blue.

(01 $l$ ) and (02 $l$ ) measurements were fitted by Gaussian functions, yielding a FWHM of 0.055 and 0.058  $\text{\AA}^{-1}$  for the first and the second order rods, respectively. These values correspond to a film thickness  $t = 16.1$  and 15.2  $\text{\AA}$ , approximately equivalent to 3 TL (1 triple layer, 1 bulk TL = 5.51  $\text{\AA}$ ).

#### 4.3. Stress in FeSe on $\text{Bi}_2\text{Se}_3(0001)$

We measure the change of curvature [22,23] of the  $\text{Bi}_2\text{Se}_3(0001)$  substrate crystal upon Fe deposition on  $\text{Bi}_2\text{Se}_3$  to derive the film stress. A quartz crystal is employed to calibrate the deposited thickness. Fig. 9 shows the stress change during deposition of 0.3 ML Fe carried out at two different temperatures. In each case, the stress is observed to decrease monotonically. The negative slope of the stress curves indicates a compressive stress change, which amounts to  $-3.5 \pm 0.3$  N/m for deposition at 473 K, and to  $-2.2 \pm 0.2$  N/m for deposition at room temperature (inset of Fig. 9).

Accompanying LEED experiments confirmed the formation of FeSe in three rotational domains after deposition of Fe at 473 K, to which we can

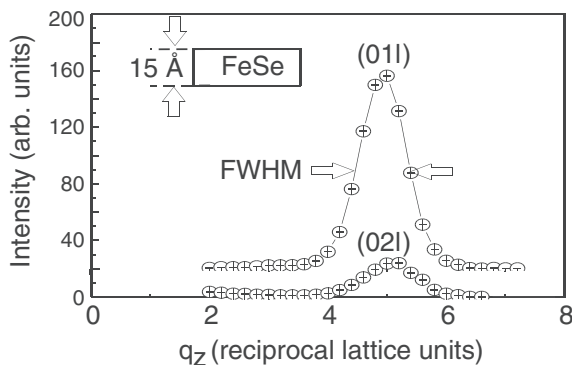


**Fig. 8.** X-ray intensity along the first (01 $l$ ) and second (02 $l$ ) order rods of the FeSe film on  $\text{Bi}_2\text{Se}_3$ . The finite full width at half maximum corresponds to a film thickness of  $t \approx 15$   $\text{\AA}$ , while the peak position is related to a lattice constant of  $c \approx 5.74$   $\text{\AA}$ . A reciprocal lattice unit equals to  $(28.64 \text{\AA})^{-1}$ .

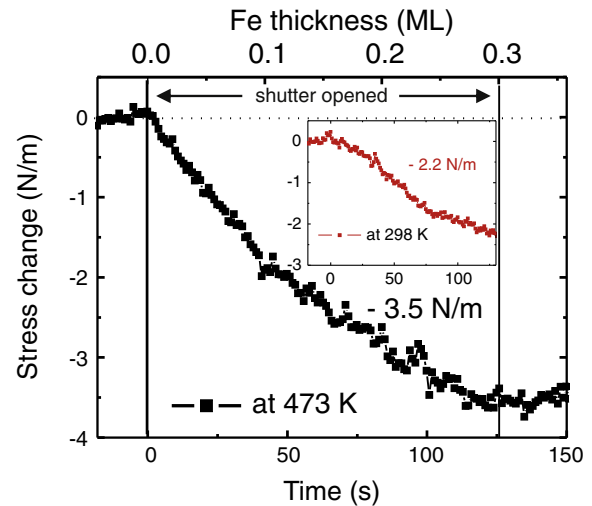


**Fig. 9.** Stress change during deposition of Fe on  $\text{Bi}_2\text{Se}_3(0001)$  at 473 K. The inset shows the induced stress change during Fe deposition at 298 K.

thus relate the stress change of  $-3.5 \pm 0.3$  N/m. In Section 5.2, we show that this stress is an order of magnitude larger than the calculated, misfit-induced stress. In contrast, Fe deposition at room temperature did not lead to a clear diffraction pattern in the LEED experiment. Hence, we ascribe the stress change of  $-2.2 \pm 0.2$  N/m to the formation of an unordered Fe- $\text{Bi}_2\text{Se}_3$  surface region.

#### 4.4. Momentum-resolved photoemission—FeSe on $\text{Bi}_2\text{Se}_3(0001)$

Momentum-resolved photoemission experiments are used to obtain a cross section through the Fermi surface of the FeSe/ $\text{Bi}_2\text{Se}_3$  system. The experiments are performed with a photoemission momentum microscope, as described in [10]. For this experiment, 1 ML of Fe was deposited at 290 K on a clean  $\text{Bi}_2\text{Se}_3$  surface and subsequently annealed to 513 K for 50 min.

The sample was located in a helium-cooled cryostat and subsequently cooled to 120 K and to 20 K. Due to the highly efficient parallelized imaging principle of the momentum microscope, both spectra displayed in Fig. 10 have been recorded within 1–2 h. The sample area contributing to our photoemission spectra has been restricted to a diameter of 20  $\mu\text{m}$ , averaging the contribution from three rotated domains  $D_1$ ,  $D_2$ , and  $D_3$ , which occur on a sub- $\mu\text{m}$  length scale, as shown in the STM image of Fig. 5 by the different orientations of the stripe patterns in FeSe. Hence, we obtain a threefold replication of the electronic structure of FeSe.

Accordingly, the surface Brillouin zone (edge length  $2\pi/a_{\text{FeSe}} = 1.67 \text{\AA}^{-1}$ ) of FeSe is indicated by dashed squares for each domain, with the color code following Fig. 7. Upon cooling to 20 K, we observe an enhancement of intensity for domain  $D_1$  over the domains  $D_2$  and  $D_3$ , nicely emphasizing the intrinsic electronic structure of FeSe in Fig. 10(b).

## 5. Discussion—FeSe nanocrystals on $\text{Bi}_2\text{Se}_3$

### 5.1. In-plane crystal structure

The starting point of our discussion is an analysis of the  $7.4 \pm 0.8$  nm periodic stripe pattern, which is reminiscent of that observed for a few atomic layer thick  $\text{Bi}_2\text{Se}_3$  film grown on a bulk FeSe crystal [17].

The different atomic spacings of  $\text{Bi}_2\text{Se}_3$  and FeSe give rise to a Moiré structure by superimposing the corresponding surface unit cells. The heterostructure represents a Moiré coincidence superlattice with period

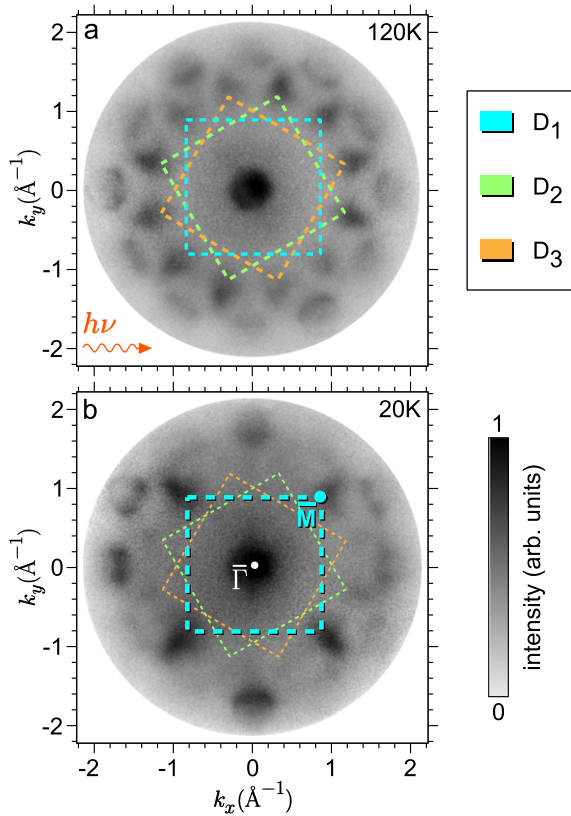


**Fig. 10.**  $k_{\parallel}$ -resolved photoemission of FeSe on  $\text{Bi}_2\text{Se}_3$  probing initial states at  $E_F$  with the He-I line ( $h\nu = 21.2$  eV, unpolarized radiation) of a laboratory gas discharge lamp. The red wavy arrow indicates the azimuth of photon incidence. The double-hemispherical energy analyzer was operated at a resolution of 0.06 eV. (a)  $T = 120$  K, (b)  $T = 20$  K.

$\lambda$ , where

$$\lambda = a_{\text{FeSe}} n = d(n + 1) \quad (1)$$

and  $a$  and  $d$  are indicated by the sketch in Fig. 11(b). With the bulk  $\text{Bi}_2\text{Se}_3$  in-plane lattice constant for the substrate,  $4.14 \text{ \AA} = d \frac{2}{\sqrt{3}}$ , eq. (1) yields with  $a_{\text{FeSe}} = 3.77 \text{ \AA}$   $n = 19.6 \pm 2.2$  for  $\lambda = 7.4 \text{ nm}$ .

We note that we observe an angle  $\alpha$  between the FeSe lattice and the Moiré stripe direction, see Fig. 11(a). This angle indicates a rotation between the  $\text{Bi}_2\text{Se}_3$  and the FeSe lattice. The model of Fig. 11(b) shows the simplest case of an alignment with vanishing rotation between the sublattices, i.e.  $\alpha = 0$ . As a result, the symmetry of the FeSe nanocrystal is lowered from tetragonal in bulk to two-fold ( $a \neq b$ ,  $\gamma = 90^\circ$ ) by proximity to the substrate. The impact of such a lowering of symmetry on the morphological and on the electronic structure remains to be determined.

Next, we discuss the LEED results. For the sake of simplicity we start from the analysis of a single FeSe domain, shown in real space in Fig. 12(a). The surface unit cell is shown by a solid blue line, while the solid red circles represent the lattice points of the trigonal  $\text{Bi}_2\text{Se}_3$  substrate in real space. Due to the symmetry of the substrate, we expect three rotated domains, and the other two domain orientations of FeSe are shown by faint blue lines in (a). They originate from the first domain by a rotation by  $120^\circ$  and  $240^\circ$ .

The resulting LEED pattern shows diffraction spots due to the trigonal substrate unit cell, and due to FeSe in three rotational domains. We calculate the resulting pattern [24] and superimpose the calculated pattern with the measured diffraction pattern in Fig. 12(b). Here, red dots

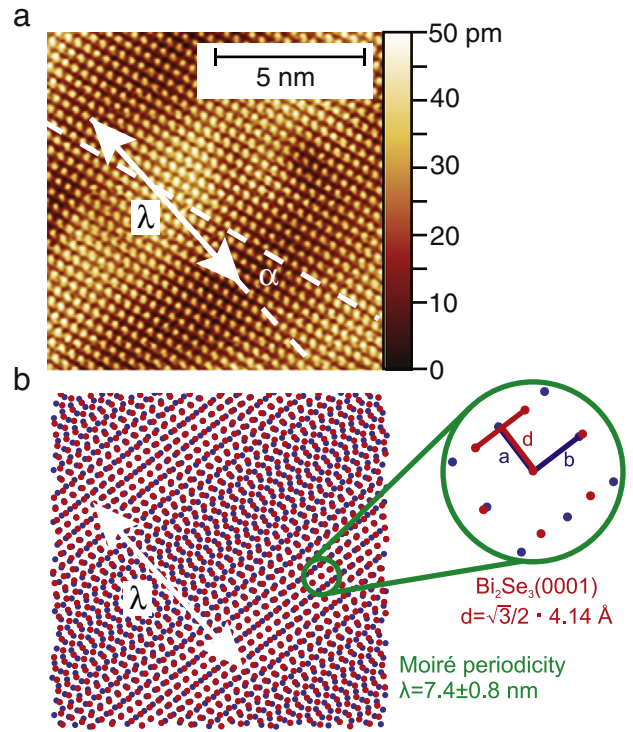


**Fig. 11.** (a) STM image of FeSe on  $\text{Bi}_2\text{Se}_3(0001)$ . A 7.4 nm periodic modulation of the apparent height of the FeSe lattice is clearly visible. The amplitude of this modulation is  $\approx 20$  pm. Image parameters:  $U = +300$  mV,  $I = 200$  pA.  $\alpha$  is the angle between the normal to the stripe pattern ridge and the FeSe lattice vector. (b) The schematic diagram presents a Moiré coincidence lattice generated by the superposition of  $\text{Bi}_2\text{Se}_3$  (red) and FeSe (blue) unit cells, each represented by a circular dot. Along the direction  $\lambda$  the FeSe unit vector  $a$  does not match the length  $d$ , see sketch at the right. A coincidence between the two lattices thus appears every  $n$  repetitions, see text for details. The period  $\lambda$ , indicated by the white arrows, characterizes this coincidence Moiré superlattice.

represent diffraction spots due to  $\text{Bi}_2\text{Se}_3(0001)$ , and blue dots are due to diffraction from FeSe in three domains.

We identify six plus six sets of FeSe spots forming inequivalent alternating equilateral triangles in the outermost ring (green and blue dashed triangles in Fig. 12(b)). The difference in area between the dashed triangles directly indicates a difference between the lengths  $a$  and  $b$ , which were introduced in (a). This difference signifies an orthorhombic symmetry for FeSe on  $\text{Bi}_2\text{Se}_3$ . Analyzing the positions of the diffraction spots we obtain  $b/a = 1.02 \pm 0.01$ , which translates to  $b_{\text{FeSe}} =$

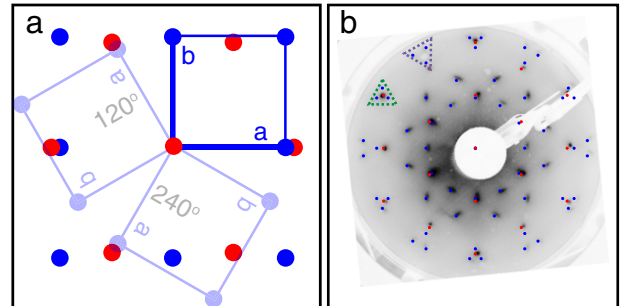


**Fig. 12.** (a) Real-space model of the surface atomic positions of  $\text{Bi}_2\text{Se}_3(0001)$  (solid red circles) and FeSe (solid blue circles) in three rotational domains. This structural model is used to calculate the LEED pattern in (b) [24]. Red and blue dots correspond to diffraction from  $\text{Bi}_2\text{Se}_3$  and FeSe, respectively. (b) Superposition of calculated LEED pattern and experimental LEED pattern at 97 eV.

$3.85 \pm 0.04 \text{ \AA}$ , where we exploit the STM Moiré analysis estimate of  $a_{\text{FeSe}} = 3.77 \pm 0.02 \text{ \AA}$ .

Thus, the in-plane lattice constants of the orthorhombic FeSe nanocrystals are obtained. In the following we use these values to calculate the expected stress in FeSe/Bi<sub>2</sub>Se<sub>3</sub>(0001).

### 5.2. Stress in FeSe on Bi<sub>2</sub>Se<sub>3</sub>(0001)

The observation of a Moiré pattern in the STM image of Fig. 6 indicates non-pseudomorphic growth. The analysis of the Moiré superlattice and of the LEED pattern yields the lattice constants  $a$  and  $b$  of the strained FeSe. The different values of  $a$  and  $b$  indicate an anisotropic in-plane strain of the FeSe nanocrystal. We calculate the stress of this strained FeSe and compare it with our experimental results.

The in-plane anisotropic strain ( $\varepsilon_1 \neq \varepsilon_2$ ) of FeSe on Bi<sub>2</sub>Se<sub>3</sub>(0001) is calculated with respect to the lattice constant of bulk FeSe. We obtain  $\varepsilon_1 = (a_{\text{FeSe}}^{\text{film}} - a_{\text{FeSe}}^{\text{bulk}}) / a_{\text{FeSe}}^{\text{bulk}} = 0$  and  $\varepsilon_2 = (a_{\text{FeSe}}^{\text{film}} - b_{\text{FeSe}}^{\text{bulk}}) / a_{\text{FeSe}}^{\text{bulk}} = +0.021$ .

First, we focus on one rotational domain of FeSe. Here,  $\varepsilon_1$  and  $\varepsilon_2$  are the strains in directions 1  $\parallel a$  and 2  $\parallel b$ , respectively,  $a_{\text{FeSe}}^{\text{bulk}} = 3.77 \text{ \AA}$  is the lattice constant of FeSe bulk [18,19], while  $a_{\text{FeSe}}^{\text{film}} = 3.77 \pm 0.02 \text{ \AA}$  and  $b_{\text{FeSe}}^{\text{film}} = 3.85 \pm 0.04 \text{ \AA}$  are the lattice constants of the FeSe film, taken from our analysis in Section 5.1.

We align directions 1 and 2 parallel to the in-plane [01 $\bar{1}$ 0] and [2 $\bar{1}$  $\bar{1}$ 0] directions of Bi<sub>2</sub>Se<sub>3</sub>, respectively. We calculate the expected stress in each direction [25]:

$$\tau_1 = \frac{Y}{1-\nu^2} \Big|_{\text{FeSe}} (\varepsilon_1 + \nu\varepsilon_2) \quad (2)$$

and

$$\tau_2 = \frac{Y}{1-\nu^2} \Big|_{\text{FeSe}} (\varepsilon_2 + \nu\varepsilon_1), \quad (3)$$

where  $Y$  and  $\nu$  are the Young modulus and the Poisson ratio of FeSe (001), with values of 73.0 GPa and 0.179 [19], respectively. Inserting the values gives an anisotropic tensile film stress of  $\tau_1 = +0.286 \text{ GPa}$  and  $\tau_2 = +1.6 \text{ GPa}$ .

The growth of FeSe on Bi<sub>2</sub>Se<sub>3</sub>(0001) is characterized by three domains of orthorhombic FeSe rotated by 0°, 120°, and 240°, see Fig. 12. Eqs. (2) and (3), give the stress for one domain, where the lattice vectors are parallel to the directions [01 $\bar{1}$ 0] and [2 $\bar{1}$  $\bar{1}$ 0] of the substrate crystal. The presence of three rotated domains requires averaging of their respective stress contributions. The procedure is outlined in the Appendix A. This analysis reveals that the calculated stress of orthorhombic FeSe on Bi<sub>2</sub>Se<sub>3</sub>(0001) is tensile isotropic in-plane stress and it amounts to  $\tau_1 = \tau_2 = +0.943 \text{ GPa}$ .

How does this calculated stress compare with the measured stress? From the measured stress during deposition of Fe on Bi<sub>2</sub>Se<sub>3</sub>, we calculate the FeSe-induced stress using  $\tau_{\text{FeSe}} = \sigma / (\theta t_F)$ , where  $\sigma$  is the measured stress change,  $\theta$  is the coverage of FeSe, and  $t_F$  is the thickness of the FeSe nanocrystals.

We deposited 0.3 ML of Fe during the stress measurement. This leads to a surface coverage of 0.1, where the local FeSe thickness is three triple layers ( $\approx 15 \text{ \AA}$ ), see Section 5.3. This gives an experimental compressive film stress of  $-23 \text{ GPa}$ .

The measured compressive stress has opposite sign and roughly a factor of twenty larger than the calculated stress for strained FeSe/Bi<sub>2</sub>Se<sub>3</sub>. Obviously, our stress calculation, which is based on epitaxial misfit alone, misses important contributions to film stress. We speculate that the high compressive stress is also due to the atomic-scale intermixing and substitutions that we suspect to take place during Fe deposition and FeSe formation. Stress measurements at 298 K show also a significant compressive stress, although no epitaxial long-range order is observed in LEED. We conclude that the epitaxial misfit of FeSe is not the only origin

of stress. Further insights are obtained from recent extended X-ray absorption fine structure (EXAFS) experiments. These studies indicate a preference for Bi in substitutional sites for Fe deposition [26]. Our results indicate, that epitaxial strain is not the dominant source of film stress. The influence by substitutional and interstitial sites should also be considered. In the next section we discuss the interface between FeSe and Bi<sub>2</sub>Se<sub>3</sub>, the thickness of the nanocrystals, and the out-of-plane strain in FeSe.

### 5.3. FeSe nanocrystals thickness

Fig. 5 reveals that FeSe islands appear either slightly lower or higher than the surrounding Bi<sub>2</sub>Se<sub>3</sub> substrate. The apparent height difference between FeSe and Bi<sub>2</sub>Se<sub>3</sub> areas is often negative,  $\Delta z = z_{\text{FeSe}} - z_{\text{Bi}_2\text{Se}_3}$ . A plausible explanation is that FeSe nanocrystals are embedded in the Bi<sub>2</sub>Se<sub>3</sub> crystal, i.e. they extend below the Bi<sub>2</sub>Se<sub>3</sub> surface.

A dedicated STM measurement enables a closer look onto the step heights occurring in an area around an FeSe nanocrystal. Fig. 13 shows a 3D representation of that STM measurement. Here, atomically resolved STM identifies the terraces as either Bi<sub>2</sub>Se<sub>3</sub> or FeSe, due to their distinctly different surface symmetries. The apparent-height profile (red line) in Fig. 13(b) presents three different levels, separated by  $\Delta z = 7.6 \text{ \AA}$  and  $1.8 \text{ \AA}$ , respectively. These values are compatible with a 3 TL thick embedded FeSe nanocrystal, as illustrated by the sketched stacking of FeSe TLs and Bi<sub>2</sub>Se<sub>3</sub> QLs.

Our SXRD experiments reveal an average lattice parameter of  $c = 5.73 \text{ \AA}$  for the thickness of one TL FeSe. This reflects a lattice expansion along the vertical direction in comparison with the FeSe bulk value ( $c^{\text{bulk}} = 5.51 \text{ \AA}$ ). This difference indicates a lattice expansion along the out-of-plane direction of  $\varepsilon_3 = +4.2\%$ .

The combined use of SXRD, LEED and STM provides insight into the peculiar growth mode resulting from the deposition of Fe on Bi<sub>2</sub>Se<sub>3</sub> and subsequent annealing. We speculate that an upper limit exists for the thickness of FeSe nanocrystals which can be prepared this way on Bi<sub>2</sub>Se<sub>3</sub>. This limit is probably given by the maximum depth from which Se atoms can be extracted from the bulk of Bi<sub>2</sub>Se<sub>3</sub> to form FeSe. This growth process is thus different from the progressive build-up of FeSe TLs obtained when co-depositing Fe and Se [27,28,29].

### 5.4. Electronic structure – Electron photoemission

The qualitative inspection of the photoelectron maps in Fig. 10 reveals a distinct symmetry of the intensity distribution of photoelectrons over  $k$ -space. The symmetry of FeSe manifests itself by four intense elongated high-intensity features at the  $\bar{M}$  points in Fig. 10(b). In a previous photoemission study [30], similar features at the  $\bar{M}$  points,

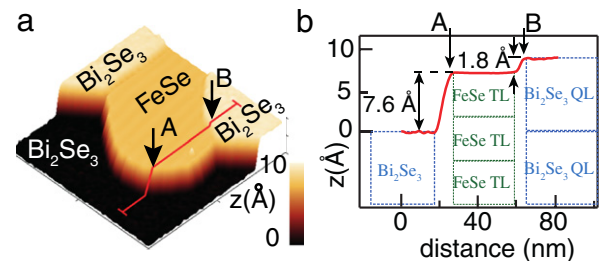


Fig. 13. (a) Constant-current STM topography image ( $100 \times 100 \text{ nm}^2$ ) of an embedded FeSe nanocrystal on Bi<sub>2</sub>Se<sub>3</sub>. (b) Line profile across the FeSe island indicates step heights of 7.6 and 1.8 Å which can be rationalized by the depicted model of the embedded FeSe nanocrystal.

observed in a single layer FeSe on SrTiO<sub>3</sub>, have been identified as electron pockets.<sup>1</sup>

A further high-intensity feature is located at  $\bar{\Gamma}$ . It has the shape of a square rotated by 45°. This contour was not present at the Fermi level in the experiment of reference [30], where the FeSe single layer is under tensile strain due to the SrTiO<sub>3</sub> substrate (lattice mismatch 3.7%). The sizable lattice strain of that system, which generally causes an energetic shift of electronic states, may well shift bands such that crossings of the Fermi level are lifted, thereby removing a Fermi surface contour.

However, the Fermi contour at  $\bar{\Gamma}$  was reproduced in a band structure calculation for bulk  $\beta$ -FeSe and characterized as hole pocket features. Similarly, photoemission experiments for FeSe single crystals showed the presence of hole pockets at  $\bar{\Gamma}$  using a photon energy of 25 eV [31]. Since in our case, the in-plane lattice constant corresponds to bulk FeSe within less than 2%, we find that the observed photoemission features are consistent with previous experimental results, confirming the presence of FeSe nanocrystals in our samples.

The maps of Fig. 10 reveal an apparent increase of intensity of one rotational domain only upon cooling from 120 to 20 K. As to the origin of this intensity enhancement after cooling to 20 K, we remark that at this temperature, adsorption of residual gases, even in UHV pressure of  $3 \times 10^{-11}$  mbar, leads to a rapid complete attenuation of the observed photoemission peaks within only a few hours. This change of the surface condition cannot be completely reversed by heating to room temperature and cooling down again. However, starting from a newly prepared FeSe thin film on Bi<sub>2</sub>Se<sub>3</sub> we reproducibly found enhanced intensity of the photoemission features belonging to D<sub>1</sub>.

Considering the symmetry of the FeSe/Bi<sub>2</sub>Se<sub>3</sub> structure, all three rotated domains of FeSe are equivalent, and none has a distinguished role. It is clear, that the preferential intensity enhancement of domain D<sub>1</sub> in photoemission can only be explained by the incident light. In particular, possible mechanisms might be:

(1) A reduced adsorption of residual gases on domain D<sub>1</sub> compared to the other two domains during cooling to 20 K caused by irradiation. Only for D<sub>1</sub>, the incident light is perpendicular to its striped spatial pattern. Subsequently, the photoemission intensity belonging to D<sub>2</sub> and D<sub>3</sub> would be suppressed compared to D<sub>1</sub>.

(2) A change in the electronic structure between 120 K and 20 K affecting the photoemission cross-section. In case of non-normally incident light, photoemission patterns recorded in a two-dimensional momentum-resolved distribution show different intensities in each of the quadrants ( $\pm k_x, \pm k_y$ ). These different intensities, in spite of probing equivalent electronic states, are due to transition matrix elements – an effect known as linear dichroism in angular distribution (LDAD). The unpolarized light which we use, can be described as an incoherent superposition of p-polarized and s-polarized light, with a stronger weight of the p-polarized component owing to the different transmission through the surface for each component. The orbitals of electronic states within the FeSe domains are aligned to the domain-specific crystalline axes, so that the incident light has a different orientation with respect to such orbitals according to the orientation of the domain. This domain-specific geometry of the photoemission results in different excitation cross-sections, e.g. different photoemission intensities. The LDAD already leads to unequal intensities of the 12 elongated features at the  $\bar{M}$  points for  $T = 120$  K (note the highest intensity along the  $k_x = -k_y$  axis). However, a possible phase transition between 120 K and 20 K, affecting the electronic structure may alter the LDAD and thus lead to the observed intensity enhancement of the  $\bar{M}$  point features belonging to domain D<sub>1</sub>. In this respect, we recall the structural phase transition reported for bulk FeSe at temperatures below 90 K [32],

introducing an orthorhombicity with in-plane lattice constants deviating by 0.4%. In our case, the Bi<sub>2</sub>Se<sub>3</sub> substrate already causes a 2% difference of the in-plane FeSe lattice constants at room temperature (see Section 4.1). Therefore, it is not a priori clear, what kind of phase transitions are present in the strained FeSe islands. Recently it has been suggested, that the structural phase transition is driven by orbital ordering [33], e.g. by lifting the degeneracy of the  $d_{yz}$  and  $d_{xz}$  orbitals. If such an electronic rearrangement drives the structural phase transition, it may as well be present in our FeSe islands, even if they are already orthorhombic at room temperature by alignment to the Bi<sub>2</sub>Se<sub>3</sub> substrate.

Further investigation of the mechanism that leads to the intensity enhancement of D<sub>1</sub> after cooling from 120 K to 20 K is a most interesting task for the future and may illuminate its relation to the superconducting phase or other kinds of electronic phase transitions occurring in FeSe.

As a final note, we emphasize, that due to the working principle of the momentum microscope, the photoemission geometry is fixed during experiment (as well as across subsequent experiments). This stands in contrast to standard ARPES (angle-resolved photoemission) experiments, where the momentum-axes (or angular axes) are scanned by rotating and tilting the sample. Additionally, the parallelized detection of two-dimensional momentum images enabled us to record the spectra shown here sufficiently fast, before considerable adsorption-related attenuation of photoemission peaks sets in. For these two reasons, the observations reported here, may have been impossible to detect in most of the previously published studies.

## 6. Conclusions and outlook

A multi-technique experimental investigation on the preparation and the characterization of Bi<sub>2</sub>Se<sub>3</sub>(0001) and on the growth of FeSe nanocrystals on Bi<sub>2</sub>Se<sub>3</sub>(0001) has been performed. We show that sputtering and annealing, with carefully adjusted annealing temperature  $T_{ann} = 673$ – $693$  K, yields pristine Bi<sub>2</sub>Se<sub>3</sub>(0001) surfaces. Bi<sub>2</sub>Se<sub>3</sub> preparation by ion bombardment and annealing cycles opens the way to perform experiments on Bi<sub>2</sub>Se<sub>3</sub> in cases, where crystal cleavage is no option. One example are curvature stress measurements, which require 0.1 mm thin substrate crystals. Here, cleavage is not possible, as a controlled separation of the crystal halves over an area of some 10 mm<sup>2</sup>, rendering a uniform sample thickness in the 0.1 mm range is beyond reach. However, we performed curvature stress measurements successfully on sputter and annealed Bi<sub>2</sub>Se<sub>3</sub>(0001) samples.

Bi<sub>2</sub>Se<sub>3</sub>(0001) is used as a template for the subsequent growth of FeSe nanocrystals by Fe deposition and annealing, or by deposition at elevated temperature. Growth of FeSe occurs with Se atoms supplied by Bi<sub>2</sub>Se<sub>3</sub> without need for an additional source of Se. The required temperature of annealing to prepare well ordered epitaxial FeSe, is within the 613–653 K range. These temperatures are lower compared to the 773 K required to obtain FeSe on SrTiO<sub>3</sub> [34].

The structural characterization of the FeSe nanocrystals by SXRD, LEED, and STM reveals an anisotropic three-dimensional strain state, where FeSe is expanded in-plane and out-of-plane. We note that this strain state cannot be realized by applying hydrostatic pressure to bulk FeSe. Spatially resolved experiments reveal FeSe nanocrystals with lateral size from few tens to hundreds nm and average thickness of 15 Å. The FeSe nanocrystals are embedded into the Bi<sub>2</sub>Se<sub>3</sub> substrate. Stress measurements during Fe deposition at 473 K reveal a film stress of  $-23$  GPa, inverted sign and much larger magnitude than expected from epitaxial misfit strain considerations. The change of film stress is possibly linked to the peculiar growth mechanism, where also deviations from an idealistic structural and elemental order in the system needs to be considered.

A key question with respect to the potentially superconducting properties of epitaxial FeSe is whether the crystal possesses a two- or a four-fold rotational symmetry in its morphological and electronic structure [35,36]. Our results reveal that the Bi<sub>2</sub>Se<sub>3</sub> substrate effectively

<sup>1</sup> The notion of electron and hole pockets refers to Fermi surface contours formed by bands which according to the curvature of their dispersion  $\frac{\partial^2 E}{\partial k^2}$  have an effective mass  $m > 0$  (electrons) or  $m < 0$  (holes) at the Fermi level.

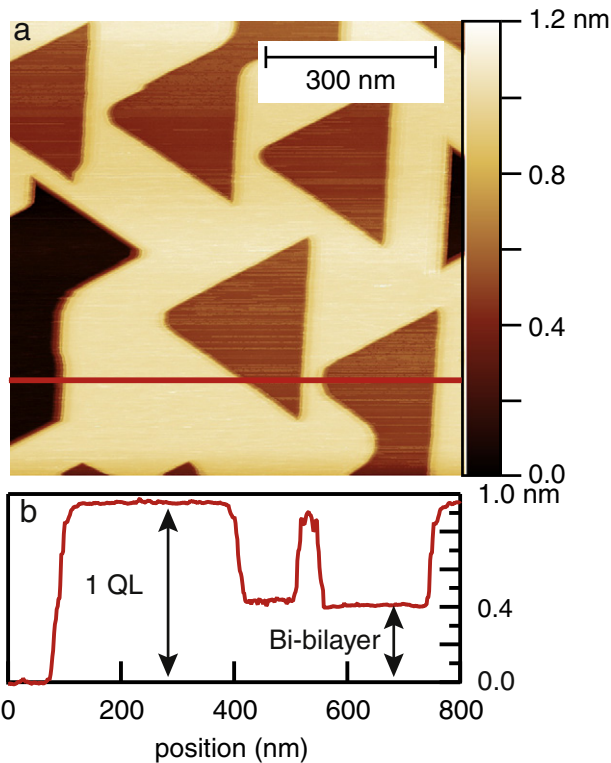


**Fig. 14.** STM image of the *in vacuo* cleaved sample without ion bombardment after three 30' long 623 K annealing processes (a).  $U = +0.4$  V,  $I_T = 200$  pA. Depressions with two distinct depths can be clearly distinguished: the depths are either 1 QL (0.95 nm) or 0.50–0.55 nm, as indicated in (b) by the line profile along the red line shown in (a).

reduces the symmetry of FeSe, and this may prove decisive for its superconducting properties.

### Acknowledgments

The  $\text{Bi}_2\text{Se}_3$  crystals used in this work have been supplied by E.V. Chulkov. The authors acknowledge R. Decker, R. Shokri, and S. Roy for the discussions, and W. Greie, H. Menge, and F. Weiss for the advanced technical support. Partial funding by DFG SFB 762 and by DFG SPP1666 (Topological Insulators) is gratefully acknowledged.

### Appendix A

We obtained remarkable surface morphologies after annealing  $\text{Bi}_2\text{Se}_3(0001)$ . Annealing of *in vacuo* cleaved crystals yields triangular depressions, which present two characteristic orientations and depths, see Section A.1. On the other hand, samples which have been ion-bombarded and subsequently annealed to  $T_{\text{ann}} = 623$  K present a peculiar long-range quasi-hexagonal modulation of the apparent height, see Section A.2.

#### A.1. The role of annealing—Surface morphology after heating to 623 K

Here we show that annealing to a low temperature of 623 K creates triangular depressions on the surface. Our observation of the change of morphology during a series of annealing steps to 623 K suggests that the depressions form by atomic evaporation from the surface. The depression formation begins with nm-sized triangular surface vacancies, which are 1 QL deep (first annealing, image not shown). These vacancy holes grow in size, while maintaining their edges orientation, and grow to a size of hundreds of nm across. Considering that their depth equals

1 QL, we expect the same termination of the freshly exposed surface at the bottom of the depression and at the uppermost layer.

More and more shallow holes (depth 0.5 nm) appear as the cumulative annealing time increases. Fig. 14(a) provides an example. These depressions are 5–5.5 Å deep, and their orientation is rotated by 180° with respect to QL-deep depressions. STM with atomic resolution inside these shallow depressions reveals a hexagonal atomic lattice with interatomic distances compatible with those of the  $\text{Bi}_2\text{Se}_3(0001)$  surface. No additional modulation in apparent height is observed. This finding is compatible with the structure of a Bi bilayer [37,38]. Thus we speculate that this preparation leads to shallow depressions which are ascribed to the presence of a Bi bilayer at the bottom of the depression.

#### A.2. Sputtering and annealing with $T_{\text{ann}} \approx 623$ K

Ion bombardment and subsequent annealing at  $T_{\text{ann}} \approx 623$  K lead to the formation of a long-range quasi-hexagonal superstructure, as shown in the constant current image of Fig. 15. Although the unit cell vectors of the superstructure are not exactly defined due to disorder in the superlattice, we can estimate their lengths to be of order 20–23 nm. On top of the long-range modulation we observe sub-nm wide, circularly shaped, irregularly arranged protrusions with an apparent height of  $\approx 0.5$  Å. The protrusions cannot be manipulated by the STM tip. This may suggest that they are not adsorbates on the otherwise ideal  $\text{Bi}_2\text{Se}_3$  surface, but rather atoms embedded in the QL. We propose two tentative models for the observed quasi-hexagonal modulation of the apparent height:

- a Moiré pattern given by the lattice mismatch of the uppermost  $\text{Bi}_2\text{Se}_3$  quintuple layer with respect to the underlying bulk crystal. Weak van-der-Waals interaction between the uppermost QL and the next could result in a non-pseudomorphic structure. A periodicity of 20 nm between regions of equivalent height corresponds to an in-plane lattice mismatch of 2% on average. Indeed, the observed subsurface defects could be responsible for such an in-plane lattice mismatch.
- a subsurface network of dislocations. Articles by M. Schmid and co-authors present an example of similar a structure in a metal alloy, which was formed by preferential sputtering of one of the components [39,40]. A distortion network results for relatively high dislocation densities.

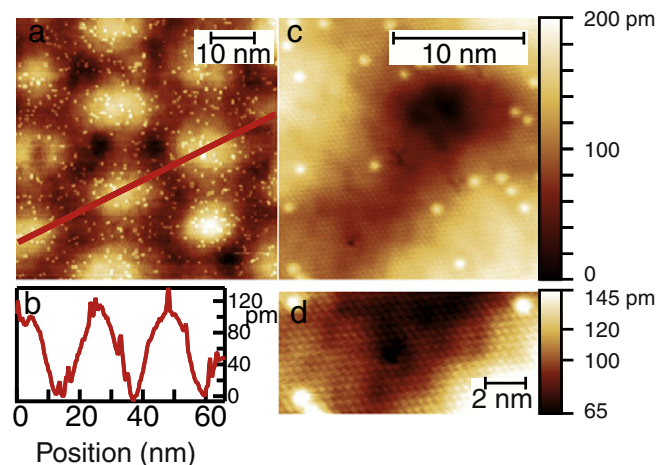


**Fig. 15.** STM image of  $\text{Bi}_2\text{Se}_3$  sputtered and subsequently annealed to 623 K (a).  $U = +500$  mV,  $I_T = 1$  nA. A quasi-hexagonal superstructure with 20–23 nm periodicity is visible in constant current images. The apparent height amplitude is approximately 100 pm, as revealed by the line scan of (b). On top of this modulation, some protrusions appear with an apparent height of 40 pm. Atomic resolution STM imaging of the surface in (c) and (d) shows a hexagonal surface corrugation.  $U = +0.5$  V,  $I_T = 0.7$  nA.

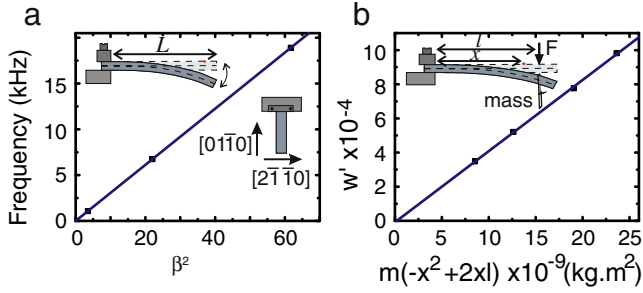


**Fig. 16.** Experimental determination of the Young modulus of a  $\text{Bi}_2\text{Se}_3(0001)$  crystal. (a) Plot of the resonance frequencies as a function of the mode constant ( $\beta^2$ ). The slope of the curve is  $306.35 \pm 0.02$  Hz. (b) Plot of the change of slope of the crystal ( $w'$ ). The slope of the curve is  $4.1 \times 10^4 \pm 7.1 \times 10^2$  kg  $\text{m}^2$ .

Further work is required to elucidate the physical origin of these peculiar surface morphologies.

### A.3. Young modulus and Poisson ratio of $\text{Bi}_2\text{Se}_3(0001)$

The quantitative analysis of the optical crystal curvature stress measurement [22,23] requires the biaxial modulus of the substrate,  $Y/(1-\nu)$ , as input to convert the substrate curvature  $1/R$  into a film stress  $\tau_F$  via

$$\Delta(\tau_F \cdot t_F) = \frac{Yt^2}{6(1-\nu)} \Big|_{\text{Bi}_2\text{Se}_3} \Delta \frac{1}{R}, \quad (4)$$

with the thicknesses of the film  $t_F$  and of the substrate  $t = 0.1$  mm, the Young modulus  $Y$  and the Poisson ratio  $\nu$ .

To the best of our knowledge, the experimental value of the Young modulus  $Y$  of  $\text{Bi}_2\text{Se}_3$  has not been reported before. Therefore we derive it experimentally in two ways: i) from the flexural vibration frequencies of the cantilever substrate, and ii) from the weight-induced deflection of a  $\text{Bi}_2\text{Se}_3$  cantilever substrate. These experiments are further elucidated in the Appendix A. We obtain the Young modulus for  $\text{Bi}_2\text{Se}_3(0001)$  as  $Y = 47 \pm 9$  GPa. The Poisson ratio  $\nu$  is not directly accessible by the measurements i) and ii). Hence, we use  $\nu = 0.241$ , reported for the related compound  $\text{Bi}_2\text{Te}_3(0001)$  [41], as the best available estimate in Eq. (4).

#### A.3.1. Experimental determination of the Young modulus of $\text{Bi}_2\text{Se}_3(0001)$

We exploit flexural vibrations and mass-induced deflections of cantilevered  $\text{Bi}_2\text{Se}_3(0001)$  samples to derive the Young modulus experimentally.

The resonance frequency of flexural vibrations of a cantilever is given by [42]:

$$f_n = \frac{\beta_n^2}{2\pi} \sqrt{\frac{YI}{mL^4}}, \quad (5)$$

where  $m$  is the mass,  $L$  is the length of the sample,  $Y$  is the Young modulus,  $\beta_n$  is a mode constant ( $\beta_1 = 4.694$ ,  $\beta_2 = 7.855$ , and  $\beta_3 = 10.996$ ), and  $I$  is the areal moment of inertia ( $I = bt^3/12$  [43], where  $b$  and  $t$  are the width and thickness of the sample). Thus, the Young modulus is derived from a measurement of the resonance frequency of the cantilever sample by the optical deflection measurement. The second technique exploits the deflection of the cantilever upon application of a known force at a given position of the cantilever. We measure the change of slope  $w'$  of the cantilever deflection upon loading the cantilever with a known mass. We use [44]:

$$w'(x) = \frac{Fl^2}{2YI} \left( -\frac{x^2}{l^2} + \frac{2x}{l} \right), \quad (6)$$

where  $F$  is the force due to the attached weight,  $Y$  is the Young modulus,  $I$  is the areal moment of inertia,  $l$  and  $x$  are the lever arm length of the mass and the position of the slope measurement, respectively. See sketch in Fig. 16(b).

Fig. 16(a) gives the plot of three resonance frequencies measured on a  $\text{Bi}_2\text{Se}_3$  crystal as a function of mode constant  $\beta^2$ . Fig. 16(b) gives the change of slope due to loading the cantilever with four different weights.

We obtain a Young modulus for  $\text{Bi}_2\text{Se}_3(0001)$  of  $47 \pm 9$  GPa. The Poisson ratio  $\nu$  cannot be determined this way, and we choose the reported value of the related compound  $\text{Bi}_2\text{Te}_3(0001)$  of  $\nu = 0.241$  [41].

This relatively small value of  $Y$  is not unexpected for this peculiar structure.  $\text{Bi}_2\text{Te}_3$  has a similar layered structure and the experimental Young modulus is 54.2 GPa, in close agreement with a theoretical result ( $Y = 51.4$  GPa) [45]. We see that these layered materials are very soft in comparison with metals such as Ir, where  $Y = 634$  GPa [46].

### A.4. Averaging film stress over three rotational domains

The observation of three rotational domains requires averaging of stress contributions of the three structural domains. We use the transformation matrix  $a_{ij}$  in order to obtain the stress along the length and the width of the crystal. The stress tensor  $\tau_{ij}$  can be written as:

$$\tau_{ij} = \begin{pmatrix} \tau_1 & 0 & 0 \\ 0 & \tau_2 & 0 \\ 0 & 0 & 0 \end{pmatrix}.$$

To obtain the stress contribution from the rotated domains, we have to apply a tensor transformation, using [25]:

$$\tau'_{ij} = a_{ij}^T \tau_{ij} a_{ij}, \quad (7)$$

where  $\tau'_{ij} = a_{ij}^T \tau_{ij} a_{ij}$ , is the stress tensor of the rotated domain,  $a_{ij}$  and  $a_{ij}^T$  are the transformation matrix and its transposed, respectively. The transformation matrix is written:

$$a_{ij} = \begin{pmatrix} \cos\theta & -\sin\theta & 0 \\ \sin\theta & \cos\theta & 0 \\ 0 & 0 & 1 \end{pmatrix},$$

where  $\theta$  is the angle between the domains (d1, d2, d3):  $\theta = 120^\circ$  for domain 2, and  $\theta = 240^\circ$  for domain 3. We obtain:

$$\tau^{d1} = \begin{pmatrix} +0.286 & 0 & 0 \\ 0 & +1.6 & 0 \\ 0 & 0 & 0 \end{pmatrix} \text{ GPa},$$

$$\tau^{d2} = \begin{pmatrix} +1.272 & -0.5688 & 0 \\ -0.5688 & +0.6149 & 0 \\ 0 & 0 & 0 \end{pmatrix} \text{ GPa},$$

$$\tau^{d3} = \begin{pmatrix} +1.272 & +0.5688 & 0 \\ +0.5688 & +0.6149 & 0 \\ 0 & 0 & 0 \end{pmatrix} \text{ GPa}.$$

The total averaged stress of all three domains ( $\tau_{ij}^{\text{total}}$ ) is given by:

$$\tau_{ij}^{\text{total}} = \frac{\tau_{ij}^{d1} + \tau_{ij}^{d2} + \tau_{ij}^{d3}}{3}, \quad (8)$$

where the superscripts d1, d2, and d3 identify the first, second, and third domains, respectively. The resulting stress is isotropic in-plane

$$\tau_{12}^{\text{total}} = \begin{pmatrix} +0.943 & 0 & 0 \\ 0 & +0.943 & 0 \\ 0 & 0 & 0 \end{pmatrix} \text{ GPa.}$$

The orthorhombic FeSe on Bi<sub>2</sub>Se<sub>3</sub> gives rise to three stress domains which lead to an average calculated isotropic in-plane tensile stress of +0.93 GPa.

## References

- [1] L. Fu, C. Kane, *Phys. Rev. Lett.* 100 (2008) 096407, <http://dx.doi.org/10.1103/PhysRevLett.100.096407> (doi:10.1103/PhysRevLett.100.096407).
- [2] Z.-Z. Li, F.-C. Zhang, Q.-H. Wang, *Sci. Rep.* 4 (2014) 6363, <http://dx.doi.org/10.1038/srep06363> (doi:10.1038/srep06363).
- [3] F. Wilczek, *Nature Phys.* 5 (2009) 614, <http://dx.doi.org/10.1038/nphys1380> (doi:10.1038/nphys1380).
- [4] S. Urazhdin, D. Bilc, S.H. Tessmer, S.D. Mahanti, T. Kyratsi, M.G. Kanatzidis, *Phys. Rev. B* 66 (2002) 161306, <http://dx.doi.org/10.1103/PhysRevB.66.161306> (doi:10.1103/PhysRevB.66.161306).
- [5] S. Kim, M. Ye, K. Kuroda, Y. Yamada, E.E. Krasovskii, E.V. Chulkov, K. Miyamoto, M. Nakatake, T. Okuda, Y. Ueda, K. Shimada, H. Namatame, M. Taniguchi, A. Kimura, *Phys. Rev. Lett.* 107 (2011) 056803, <http://dx.doi.org/10.1103/PhysRevLett.107.056803> (doi:10.1103/PhysRevLett.107.056803).
- [6] Y.S. Hor, A. Richardella, P. Roushan, Y. Xia, J.G. Checkelsky, A. Yazdani, M.Z. Hasan, N.P. Ong, R.J. Cava, *Phys. Rev. B* 79 (2009) 195208, <http://dx.doi.org/10.1103/PhysRevB.79.195208> (doi:10.1103/PhysRevB.79.195208).
- [7] <http://www.polytec-pt.com> Polytec pt: Resbond 931c. URL <http://www.polytec-pt.com>.
- [8] <http://www.lumasenseinc.com> Pyrometer impac ip 140.
- [9] C.M. Schlepütz, R. Herger, P.R. Willmott, B.D. Patterson, O. Bunk, C. Brönnimann, B. Henrich, G. Hilsen, E.F. Eikenberry, *Acta Cryst. A* 61 (2005) 418, <http://dx.doi.org/10.1107/S0108767305014790> (doi:10.1107/S0108767305014790).
- [10] C. Tusche, A. Krasnyk, J. Kirschner, Spin Resolved Bandstructure Imaging With a High Resolution Momentum Microscope, 2015 <http://dx.doi.org/10.1016/j.ultramic.2015.03.020> (Ultramicroscopy in press).
- [11] C. Chen, *Introduction to Scanning Tunneling Microscopy*, Oxford University Press, New York, 1993.
- [12] H. Oka, O.O. Brovko, M. Corbetta, V.S. Stepanyuk, D. Sander, J. Kirschner, *Rev. Mod. Phys.* 86 (2014) 1127, <http://dx.doi.org/10.1103/RevModPhys.86.1127> (doi:10.1103/RevModPhys.86.1127).
- [13] V.V. Atuchin, V.A. Golyashov, K.A. Kokh, I.V. Korolkov, A.S. Kozhukhov, V.N. Kruchinin, S.V. Makarenko, L.D. Pokrovsky, I.P. Prosvirin, K.N. Romanyuk, O.E. Tereshchenko, *Crystal Growth & Design* 11 (12) (2011) 5507, <http://dx.doi.org/10.1021/cg201163v> (doi:10.1021/cg201163v).
- [14] C. Mann, D. West, I. Miotkowski, Y.P. Chen, S. Zhang, C.-K. Shih, Mapping the 3D surface potential in Bi<sub>2</sub>Se<sub>3</sub>, *Nat Commun* 4, <http://dx.doi.org/10.1038/ncomms3277>.
- [15] S. Roy, L. Meyerheim, H.A. Ernst, K. Mohseni, C. Tusche, G. Vergniory, M.V. Menshchikova, T.M. Otrokov, M.G. Ryabishchenkova, A.S. Aliev, Z.B. Babanly, M.A. Kokh, K.E. Tereshchenko, O.V. Chulkov, E.J. Schneider, J. Kirschner, *Phys. Rev. Lett.* 113 (2014) 116802, <http://dx.doi.org/10.1103/PhysRevLett.113.116802> (doi:10.1103/PhysRevLett.113.116802).
- [16] H. Zhang, C.-X. Liu, X.-L. Qi, X. Dai, Z. Fang, S.-C. Zhang, *Nat Phys* 5 (6) (2009) 438, <http://dx.doi.org/10.1038/nphys1270> (doi:10.1038/nphys1270).
- [17] Y. Wang, Y. Jiang, M. Chen, Z. Li, C. Song, L. Wang, K. He, X. Ma, Q.-K. Xue, J. Phys. *Condens. Matter* 24 (2012) 475604, <http://dx.doi.org/10.1088/0953-8984/24/47/475604> (doi:10.1088/0953-8984/24/47/475604).
- [18] F.-C. Hsu, J.-Y. Luo, K.-W. Yeh, T.-K. Chen, T.-W. Huang, P.M. Wu, Y.-C. Lee, Y.-L. Huang, Y.-Y. Chu, D.-C. Yan, M.-K. Wu, Proceedings of the National Academy of Sciences 105 (38) (2008) 14262, <http://dx.doi.org/10.1073/pnas.0807325105> (doi:10.1073/pnas.0807325105).
- [19] S. Chandra, A. Islam, *Physica C: Superconductivity* 470 (22) (2010) 2072, <http://dx.doi.org/10.1016/j.physc.2010.10.001> (doi:10.1016/j.physc.2010.10.001).
- [20] S. Margadonna, Y. Takabayashi, M.T. McDonald, K. Kasperkiewicz, Y. Mizuguchi, Y. Takano, A.N. Fitch, E. Suard, K. Prassides, *Chem. Commun.* (2008) 5607, <http://dx.doi.org/10.1039/B813076K> (doi:10.1039/B813076K).
- [21] J.M. Cowley, *Diffraction Physics*, North-Holland Publishing, Amsterdam, 1981.
- [22] D. Sander, J. Kirschner, *Physica Status Solidi (b)* 248 (10) (2011) 2389, <http://dx.doi.org/10.1002/psb.201147096> (doi:10.1002/psb.201147096).
- [23] J. Prempere, D. Sander, J. Kirschner, 073904-1-073904-8. *Rev. Sci. Instrum.* 83 (2012) <http://dx.doi.org/10.1063/1.4737384> (doi:10.1063/1.4737384).
- [24] K. Hermann, M. van Hove, URL <http://www.fhi-berlin.mpg.de/KHsoftware/LEEDpat>.
- [25] D. Sander, Reports on Progress in Physics 62 (5) (1999) 809, <http://dx.doi.org/10.1088/0034-4885/62/5/204> (doi:10.1088/0034-4885/62/5/204).
- [26] A. Polyakov, H.L. Meyerheim, E.D. Crozier, R.A. Gordon, K. Mohseni, S. Roy, A. Ernst, M.G. Vergniory, X. Zubizarreta, M.M. Otrokov, E.V. Chulkov, J. Kirschner, *Phys. Rev. B* 92 (2015) 045423, <http://dx.doi.org/10.1103/PhysRevB.92.045423>.
- [27] C.-L. Song, Y.-L. Wang, Y.-P. Jiang, Z. Li, L. Wang, K. He, X. Chen, X.-C. Ma, Q.-K. Xue, *Phys. Rev. B* 84 (2011) 020503, <http://dx.doi.org/10.1103/PhysRevB.84.020503> (doi:10.1103/PhysRevB.84.020503).
- [28] W. Zhang, Z. Li, F. Li, H. Zhang, J. Peng, C. Tang, Q. Wang, K. He, X. Chen, L. Wang, X. Ma, Q.-K. Xue, *Phys. Rev. B* 89 (2014) 060506, <http://dx.doi.org/10.1103/PhysRevB.89.060506> (doi:10.1103/PhysRevB.89.060506).
- [29] J.-F. Ge, Z.-L. Liu, C. Liu, C.-L. Gao, D. Qian, Q.-K. Xue, Y. Liu, J.-F. Jia, *Nature Mater.* 14 (2014) 285, <http://dx.doi.org/10.1038/nmat4153> (doi:10.1038/nmat4153).
- [30] D. Liu, W. Zhang, D. Mou, J. He, Y.-B. Ou, Q.-Y. Wang, Z. Li, L. Wang, L. Zhao, S. He, Y. Peng, X. Liu, C. Chen, L. Yu, G. Liu, X. Dong, J. Zhang, C. Chen, Z. Xu, J. Hu, X. Chen, X. Ma, Q. Xue, X.J. Zhou, *Nat Commun* 3 (2012) 931, <http://dx.doi.org/10.1038/ncomms1946> (doi:10.1038/ncomms1946).
- [31] J. Maletz, V.B. Zabolotnyy, D.V. Evtushinsky, S. Thirupathiah, A.U.B. Wolter, L. Harnagea, A.N. Yaresko, A.N. Vasiliev, D.A. Chareev, A.E. Böhrer, F. Hardy, T. Wolf, C. Meingast, E.D.L. Rienks, B. Büchner, S.V. Borisenko, *Phys. Rev. B* 89 (2014) 220506, <http://dx.doi.org/10.1103/PhysRevB.89.220506>.
- [32] T.M. McQueen, A.J. Williams, P.W. Stephens, J. Tao, Y. Zhu, V. Ksenofontov, F. Casper, C. Felser, R.J. Cava, *Phys. Rev. Lett.* 103 (2009) 057002, <http://dx.doi.org/10.1103/PhysRevLett.103.057002> (doi:10.1103/PhysRevLett.103.057002).
- [33] T. Shimojima, Y. Suzuki, T. Sonobe, A. Nakamura, M. Sakano, J. Omachi, K. Yoshioka, M. Kuwata-Gonokami, K. Ono, H. Kumigashira, A.E. Böhrer, F. Hardy, T. Wolf, C. Meingast, H.v. Löhnneysen, H. Ikeda, K. Ishizaka, *Phys. Rev. B* 90 (2014) 121111, <http://dx.doi.org/10.1103/PhysRevB.90.121111>.
- [34] Z. Li, J.-P. Peng, H.-M. Zhang, W.-H. Zhang, H. Ding, P. Deng, K. Chang, C.-L. Song, S.-H. Ji, L. Wang, K. He, X. Chen, Q.-K. Xue, X.-C. Ma, *Journal of Physics: Condensed Matter* 26 (10.1088/0953-8984/26/26/265002) (2014) 265002, <http://dx.doi.org/10.1088/0953-8984/26/26/265002> (doi:10.1088/0953-8984/26/26/265002).
- [35] C.-L. Song, Y.-L. Wang, P. Cheng, Y. Jiang, E. Li, T. Zhang, Z. Li, K. He, L. Wang, J.-F. Jia, H.-H. Hung, C. Wu, X. Ma, Q.-K. Chen, X. Xue, *Science* 332 (2011) 1410 (<http://dx.doi.org/10.1126/science.1202226> doi:10.1126/science.1202226).
- [36] S.-H. Baek, D. Efremov, J. Ok, J.M. Kim, J. van den Brink, B. Büchner, *Nature Mater.* 14 (2015) 210, <http://dx.doi.org/10.1038/nmat4138> (doi:10.1038/nmat4138).
- [37] P.M. Coelho, G.A.S. Ribeiro, A. Malachias, V.L. Pimentel, W.S. Silva, D.D. Reis, M.S.C. Mazzoni, R. Magalhães Paniago, *Nano Letters* 13 (9) (2013) 4517, <http://dx.doi.org/10.1021/nl402450b> (doi:10.1021/nl402450b).
- [38] R. Shokri, H.L. Meyerheim, S. Roy, K. Mohseni, A. Ernst, M.M. Otrokov, E.V. Chulkov, J. Kirschner, *Phys. Rev. B* 91 (2015) 205430, <http://dx.doi.org/10.1103/PhysRevB.91.205430> (URL <http://linkaps.org/doi/10.1103/PhysRevB.91.205430>).
- [39] M. Schmid, A. Biedermann, H. Stadler, P. Varga, *Phys. Rev. Lett.* 69 (1992) 925, <http://dx.doi.org/10.1103/PhysRevLett.69.925> (doi:10.1103/PhysRevLett.69.925).
- [40] M. Schmid, A. Biedermann, H. Stadler, C. Slama, P. Varga, *Applied Physics A* 55 (5) (1992) 468, <http://dx.doi.org/10.1007/BF00348334> (doi:10.1007/BF00348334).
- [41] H. Koc, A. Mamedov, E. Ozbay, Structural, elastic, and electronic properties of topological insulators: Sb<sub>2</sub>Te<sub>3</sub> and Bi<sub>2</sub>Te<sub>3</sub>, in: applications of Ferroelectric and Workshop on the Piezoresponse Force Microscopy (ISAF/PFM), 2013 IEEE International Symposium 2013 41, <http://dx.doi.org/10.1109/ISAF.2013.6748739> (doi:10.1109/ISAF.2013.6748739).
- [42] M. Hopcroft, W. Nix, T. Kenny, What is the Young's Modulus of Silicon?, *Microelectromechanical Systems Journal* of 19 (2) (2010) 229, <http://dx.doi.org/10.1109/JMEMS.2009.2039697> (doi:10.1109/JMEMS.2009.2039697).
- [43] L. Landau, E.M. Lifshitz, *Theory of Elasticity, Second, Revised and Enlarged Edition, Vol. 7 of Course of Theoretical Physics*, Pergamon Press, 1970.
- [44] W. Schnell, D. Gross, W. Hauger, *Technische Mechanik. Band 2: Elastostatik*, 6th Ed. Springer-Verlag, 1998.
- [45] B.-L. Huang, M. Kaviani, *Phys. Rev. B* 77 (2008) 125209, <http://dx.doi.org/10.1103/PhysRevB.77.125209> (doi:10.1103/PhysRevB.77.125209).
- [46] Z. Tian, D. Sander, J. Kirschner, *Phys. Rev. B* 79 (2) (2009) 024432, <http://dx.doi.org/10.1103/PhysRevB.79.024432> (doi:10.1103/PhysRevB.79.024432).